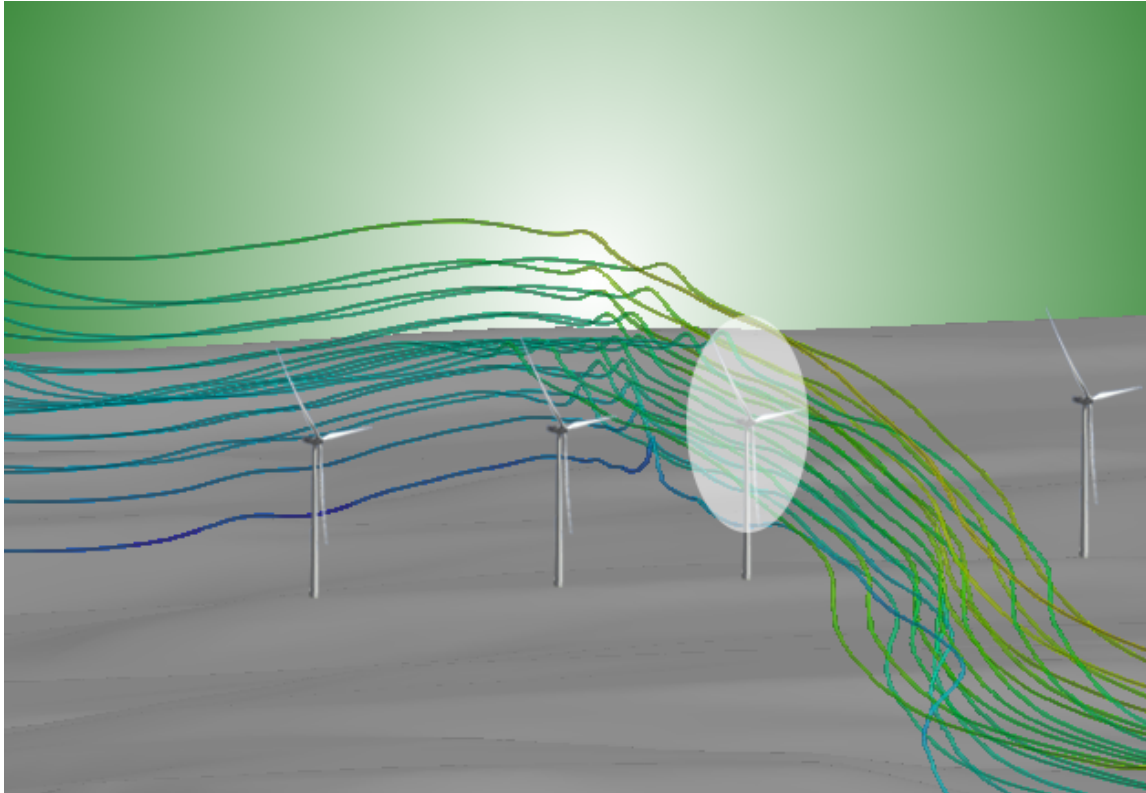




CHALMERS



Turbulence Wind Flow Modeling in Complex Terrain

A Comparison Between a Linear Model, a CFD Model and
a NWP Model

Master's thesis in Applied Mechanics

JIMMY BENGTSSON

MASTER'S THESIS IN APPLIED MECHANICS

Turbulence Wind Flow Modeling in Complex Terrain

A Comparison Between a Linear Model, a CFD Model and a NWP Model

JIMMY BENGTTSSON

Department of Applied Mechanics
Division of Fluid Mechanics
CHALMERS UNIVERSITY OF TECHNOLOGY
Göteborg, Sweden 2015

Turbulence Wind Flow Modeling in Complex Terrain
A Comparison Between a Linear Model, a CFD Model and a NWP Model
JIMMY BENGTTSSON

© JIMMY BENGTTSSON, 2015

Master's thesis 2015:46
ISSN 1652-8557
Department of Applied Mechanics
Division of Fluid Mechanics
Chalmers University of Technology
SE-412 96 Göteborg
Sweden
Telephone: +46 (0)31-772 1000

Cover:

Illustration of the simulations in STARCCM+ showing streamlines, wind turbines has been edited into the figure to make it more visual.

Chalmers Reproservice
Göteborg, Sweden 2015

Turbulence Wind Flow Modeling in Complex Terrain
A Comparison Between a Linear Model, a CFD Model and a NWP Model
Master's thesis in Applied Mechanics
JIMMY BENGTTSSON
Department of Applied Mechanics
Division of Fluid Mechanics
Chalmers University of Technology

ABSTRACT

In this thesis a comparison in wind resources predictions has been made for three different models. Predictions were made for a planned wind farm located at Skottfjället on the west coast of Sweden. Simple linear models have shown difficulty in predicting the wind resource for terrain that are forested and hilly. This thesis concludes that for Skottfjället, which is hilly and forested, the linear model results were not accurate and that predictions using computational fluid dynamics (CFD) and numerical weather prediction (NWP) models can increase the accuracy. The mean wind speed profiles has been used for the main analysis when making cross predictions and model comparisons with measurements. Further, an annual production estimation has been performed for the whole wind farm, which showed that the linear model compared to the CFD model appeared more random than accurate.

Keywords: Turbulence, wind-power, siting, meteorology, complex terrain.

ACKNOWLEDGEMENTS

First I would like to thank my supervisors Lars Davidson (Chalmers), Jon Angelbratt (Göteborg Energi) and Bastian Nebenführ (Chalmers) for guidance and support whenever help was needed. I would also like to thank Stefan Söderberg and Magnus Baltscheffsky at WeatherTech for performing model runs and helping me with questions concerning the WRF model. Furthermore, I would like to thank Ellinor Hultmark for good discussions concerning the subject and AWS Truepower for providing me with a free license of the Windographer program for measurement analysis. Finally, I would like to thank all my classmates for all the good times we have spent together.

ABBREVIATIONS

AEP - Annual Energy Production
AGL - Above Ground Level
ARW - Advanced Research WRF
ASL - Above Sea Level
CFD - Computational Fluid Dynamics
ECMWF - European Center for Medium-range Weather Forecasts
GIS - Geographical Information System
NMM - Non-hydrostatic Mesoscale Model
NWP - Numerical Weather-Prediction
PBL - Planetary Boundary Layer
RANS - Reynolds-Averaged Navier-Stokes
SLU - Sveriges Lantbruksuniversitet
SODAR - Sonic Detection And Ranging
WAsP - Wind Atlas Analysis and Application Program
WRF - Weather Research and Forecasting

LIST OF FIGURES

Figure

1.1	Wind power production in Sweden from 2001-2013 (SCB 2014).	1
3.1	The geographical location of Skottfjället where the wind farm is located. The terrain map is extracted from the Sveriges Lantbruk Universitet (SLU) database (SLU 2015a). The red rectangle marks the zoom up figure 3.2.	7
3.2	Zoomed up figure of Skottfjället including the wind farm layout. Red circles represent wind turbines and red triangles indicate measurement sites.	8
3.3	Wind distributions at 100 m for the SODAR time series of BRN2013, BRN and WWH.	9
3.4	Terrain and mesh for STARCCM+.	13
3.5	Example of the wind flow for 0° wind direction after 800 iterations. The left boundary is the east boundary and the downstream boundary is the south boundary. These boundaries show the vector field in the north to south direction. Velocity streamlines are shown passing through the wind turbines. The wind turbines are placed in the center of the domain although they are not visible.	14
3.6	Comparison of the wind profiles for different cell sizes. The left panel shows the result using OpenWind and the right panel shows the result using STARCCM+.	16
4.1	Comparison of the simulated wind profiles in STARCCM+ using two different roughness lengths for the forest and buildings. The wind profiles for STARCCM+ are calculated with the measurement from the SODAR BRN2013 at the BRN location.	17
4.2	Comparison of the simulated wind profiles in OpenWind using two different roughness lengths for the forest and buildings. The profiles are calculated with the measurement from the SODAR BRN2013 at the BRN location.	18
4.3	Comparison of the simulated wind profiles in STARCCM+, OpenWind, WRF with measurement data from the SODAR BRN2013 at the location of BRN.	19
4.4	Comparison of the simulated wind profiles in STARCCM+, OpenWind, WRF with measurement data from the SODAR WWH at the location of WWH. STARCCM+ and OpenWind are simulated using BRN2013 100 m mean wind speed.	19
4.5	Terrain height of Skottfjället. The left panel shows the real terrain height retrieved from Metria (Metria 2015). The right panel shows how the terrain height is simulated in the WRF model. White dots represent wind turbines and black squares represents the SODARS WWH and BRN.	20
4.6	Comparison of the mean velocity profiles for four chosen wind turbine locations. Upper left panel is the location of the wind turbine T4, upper right panel is the location of the wind turbine T13, lower left panel is the location of the wind turbine T18 and lower right panel is the location of the wind turbine T20. Coordinates for these wind turbines can be found in Table 3.1 and placement inside the wind farm can be seen in Figure 3.2.	21
4.7	Comparison of the simulated wind profiles in STARCCM+, OpenWind, WRF and STARCCM+ using WRF as input, with measurement data from the SODAR WWH at the location of WWH.	22
4.8	Cross prediction in STARCCM+. Wind profiles are simulated from SODAR WWH to SODAR BRN and from SODAR BRN to SODAR WWH.	22
4.9	Cross prediction in OpenWind. Wind profiles are simulated from SODAR WWH to SODAR BRN and from SODAR BRN to SODAR WWH.	23
6.1	Installation of the WWH SODAR.	25
6.2	Installation of the BRN SODAR.	25
6.3	Installation of the meteorological mast.	25

LIST OF TABLES

Table

2.1	Empirical constants in the $k-\varepsilon$ model. The modified constants are tuned for an atmospheric flow (Mandas et al. 2004).	6
3.1	Coordinates in RT90 format for the two SODAR measurement sites and the 13 turbines used in this report.	7
3.2	Shows names of the different time series for the SODAR measurements used in this study. . . .	9
3.3	Roughness length, z_0 [m]. For the forests and buildings two different roughness lengths were used (Dellwik, Arnqvist, et al. 2014), resulting in two roughness maps.	10
3.4	Power and trust curves for Vestas V90 2MW. Hub height 105 m and rotor diameter 45 m. Power and thrust values are given for a constant density of 1.225 kg/m^3 . The cut-in wind speed is 4 m/s and the cut-off wind speed is 25 m/s (Vestas 2010).	12
3.5	Reference velocity at 100 m, 1 m/s bin size and for 12 different sectors. Data was extracted from SODAR BRN in the period 2013-01-01 – 2014-01-01. The occurrences are based on the total number of times the SODAR registered a wind speed inside each 30° sector.	13
3.6	The probability that the wind is coming from a certain wind direction for BRN2013, BRN and WWH time series.	15
3.7	Computational demand for the three models.	16
4.1	The root mean square error for the wind speed profiles at the BRN location. The root mean square error for all three models are compared with the BRN2013 measurement data. The errors are calculated using the mean wind speeds at 60,80,120,140 m. The 100 m mean wind speed has not been included since OpenWind and STARCCM+ are defined through this value.	18
4.2	The root mean square error for the velocity profiles at the WWH location. The root mean square error for all three models are compared with the WWH measurement data. The errors are calculated using the mean velocities at 60,80,100,120 m.	20
4.3	Annual predicted energy production for each wind turbine [MWh/year]. Comparison between OpenWind, STARCCM+ and WindPRO.	23
4.4	The total annual predicted energy production for all 13 wind turbines.	23
4.5	The RMSE calculated as the difference between STARCCM+ and OpenWind for the 13 turbines.	23
6.1	Mean wind speed at 100 m given for all 13 wind turbines. All results are in m/s.	26
6.2	Maximum, minimum and mean wind speed at 100 m for all 13 wind turbine locations.	26
6.3	Setting for the virtual disk in STARCCM+ using 1D momentum. Except from the actual information from the wind turbine the setting for the virtual disk are specified according to the user guide for the 1D momentum method (CD-Adapco 2012).	26

CONTENTS

Abstract	i
Acknowledgements	i
Abbreviations	iii
List of Figures	iv
List of Tables	v
Contents	vii
1 Introduction	1
2 Theory	3
2.1 Meteorological boundary layer theory	3
2.1.1 The roughness sublayer	4
2.1.2 The surface layer	4
2.1.3 The Ekman layer	4
2.1.4 The geostrophic wind	4
2.1.5 Atmospheric stability	4
2.1.6 Weibull distribution	5
2.2 Reynolds-averaged Navier-Stokes equations	5
2.3 Turbulence models	5
2.3.1 k- ϵ model	6
2.3.2 Turbulence intensity	6
3 Method	7
3.1 Measurements	8
3.2 OpenWind	9
3.2.1 Set-up	9
3.2.2 Creating a windmap	10
3.2.3 Calculating the annual energy production	11
3.3 STARCCM+	11
3.3.1 Set-up	11
3.3.2 Calculating the mean free velocity	13
3.3.3 Calculating the annual energy production	14
3.4 WRF	15
3.5 WindPRO	15
3.6 Limitations	15
4 Result and discussion	17
4.1 Model comparison	17
4.2 Cross prediction	21
4.3 Production estimation	21
5 Conclusion	24
6 Appendix A	25
References	27

1 Introduction

Environmental threats due to an increased CO_2 emission have created a demand for renewable energy sources. During the 1980s the wind-power industry flourished and this dramatically increased the development of new wind turbines (Petersen et al. 1997). The development of prediction methods for the overall wind resource at a possible wind site also increased and during the 1990s, the first prediction model was introduced (Petersen et al. 1997). The wind-power production in Sweden has increased exponentially in the new millennium (see Figure 1.1) and in recent years, it has even become common for wind-power companies to build wind farms inside forests. The remoteness from inhabited places and the development of larger hub heights have made this an alternative. Inside forests, the turbulence increases, making the prediction of the wind-flow more complicated. The wind-flow effects from forests on wind turbines is a relatively new research field and a lot of research is performed by the Swedish Wind Power Technology Center (SWPTC 2015).

As the wind-power industry has expanded in the recent years, more computer programs being able to perform the wind analysis are developed. One of the most widely used softwares is called Wind Atlas Analysis and Application Program (WAsP) (Mortensen et al. 1993) and is based on the wind-atlas model (Troen and Lundtang Petersen 1989). These models solve flow equations, which has been linearised, in order to simulated the wind resource. Linear models cannot simulate detached flow and recirculation (Stuart 2004). Hence, this will give problems when the terrain is hilly. In recent years computational fluid dynamics (CFD) models have become more common when performing a wind resource analysis (Stuart 2004; Corbett et al. 2012; Manning et al. 2011). With a CFD model the flow is solved with non-linear equations and can account both for detached flow and recirculation. Besides the development of modeling softwares a whole new discipline in meteorology has arisen, namely wind-power meteorology, which is a mixture of boundary-layer meteorology, geology and climatology (Petersen et al. 1997). In wind-power meteorology, one takes into account the boundary layer characteristics, the terrain and evaluate these over annual timescales.

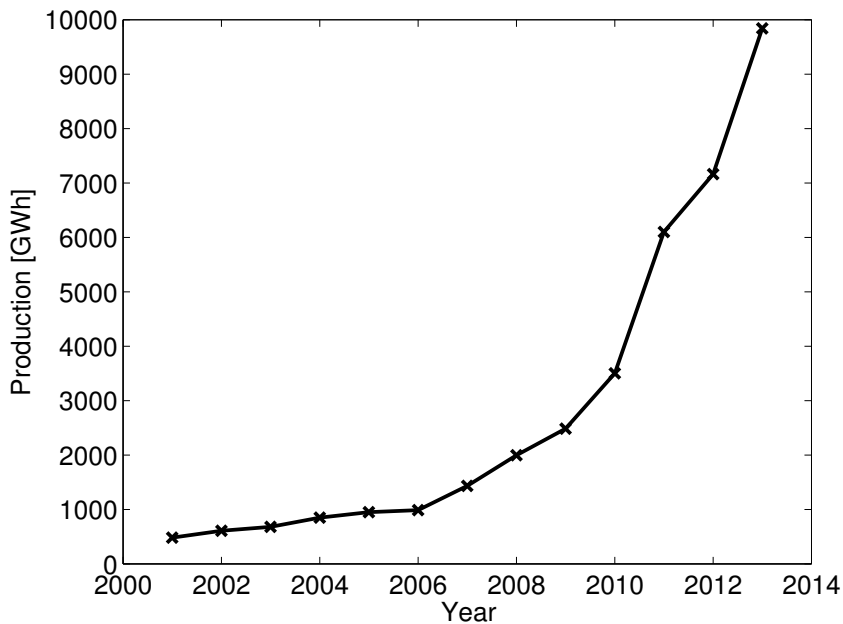


Figure 1.1: Wind power production in Sweden from 2001-2013 (SCB 2014).

Before constructing a wind farm, production estimations are performed based on the expected wind resource at the farm location. To get a good estimate of the production, meteorological masts are placed in the area of interest. The wind data are then used in computer softwares to calculate the annual production. Most wind-power softwares also take into account terrain elevation, surface roughness and atmospheric stability.

The aim of this thesis is to simulate the wind field at a wind site using three different models and comparing their prediction potential. The first model is OpenWind basic, which is a linear, open-source model, similar to WAsP. The second model, STARCCM+, is a commercial CFD software and the third model is the Weather

Research and Forecasting (WRF) model, which is a mesoscale numerical weather-prediction (NWP) model. All models were chosen for their differences in describing the wind flow. The simplest model to use was OpenWind and the hardest most computer power demanding model was the WRF model.

Göteborg Energi has been using the computer software WAsP as a wind-resource analysis program. Using the WAsP program, they have performed a cross prediction between two different measurements inside the planned wind farm. This cross prediction showed a large difference between the prediction and observations, making them question the reliability of the model. This resulted in the investigation of other models, which may be able to make better predictions.

In order to get accurate predictions using WAsP, it has been shown (Bowen and Mortensen 1996) that the measuring site and the prediction site should have the same weather, the atmospheric should be neutrally stable, the terrain should not be hilly or mountainous and that the measurement data are validated.

The accuracy and limitations of the WAsP model has further been tested in the research article by Dellwik et al. 2006. They tested different forest situations and compared the WAsP model with measurements at 15-60 m. In most cases the model overpredicted the actual wind-speed. The planned wind farm used in this thesis is situated in a hilly and forested landscape making the prediction capabilities of linear models like WAsP uncertain. Comparing three models with different ways of predicting the wind-resource, the intention is to find which model that is the most accurate in this hilly and forested landscape.

2 Theory

2.1 Meteorological boundary layer theory

The behavior of the atmosphere can be determined by seven equations: the equation of state, the first law of thermodynamics, the three components of the momentum equation (Newton's 2nd law) and the continuity equation (mass and water substances) (Petersen et al. 1997). Inside the atmosphere, there are motions occurring at scales around one mm to 10^6 m (Petersen et al. 1997). Resolving all of these scales is not possible and instead one includes terms with scales that are relevant for the flow that one investigates. Inside the boundary layer of the earth (often referred to as the planetary boundary layer (PBL)), turbulence and friction play an important role and the length scales are of the order of millimeters.

“The boundary layer is defined as the part of the troposphere that is directly influenced by the presence of the earth's surface, and responds to the surface forcing with a time scale of about an hour or less” (Stull 1988)

The boundary layer over a flat ground can be divided into three different layers, all with their own specific conditions. Closest to the ground, one finds the viscous sub-layer. The height of this layer is usually not larger than a few millimeters (Emeis 2012). Inside this layer, the wind flow is laminar and since it is so close to the ground, it does not affect the wind flow around the wind turbine. Above this layer, a surface layer exists. This layer can stretch as far as 100 m above ground and forces due to turbulent viscosity dominate within this layer (Emeis 2012). Through this layer, the wind increases rapidly with height and due to its extent, it has large effects on the wind turbines. Moving even further away from the surface, one enters the Ekman layer, which covers almost 90% of the planetary boundary layer (Emeis 2012). Here, the wind direction and wind speed is determined by the Coriolis force, the frictional force and the pressure force.

Above the PBL, the wind conditions are described by the geostrophic wind, which is balanced by the pressure gradient and the Coriolis force. If a forest is present, one more layer is introduced, the roughness sublayer, situated in-between the viscous sublayer and the surface layer (Dellwik, Landberg, and Jensen 2006). This layer is characterized by coherent turbulent motions. To analyze the wind field of the earth, meteorologists use a special form of the momentum equation (Holton and Hakim 2013).

$$\frac{Du}{Dt} - fv + f^*w + \frac{uw}{a} - \frac{uv \tan(\phi)}{a} = -\frac{1}{\rho} \frac{\partial p}{\partial x} + F_{rx}, \quad (2.1)$$

$$\frac{Dv}{Dt} + fu + \frac{vw}{a} + \frac{u^2 \tan(\phi)}{a} = -\frac{1}{\rho} \frac{\partial p}{\partial y} + F_{ry}, \quad (2.2)$$

$$\frac{Dw}{Dt} - 2\Omega u \cos(\phi) - \frac{u^2 + v^2}{a} = -\frac{1}{\rho} \frac{\partial p}{\partial z} - g + F_{rz}, \quad (2.3)$$

$$\frac{D}{Dt} = \frac{\partial}{\partial t} + v_i \frac{\partial}{\partial x_i}. \quad (2.4)$$

Here u and v are the horizontal wind components, w is the vertical wind component, f is the horizontal Coriolis parameter, f^* is the vertical Coriolis parameter, a is the radius of the earth, ϕ is the latitude, F_{rx}, F_{ry}, F_{rz} are the three components of the frictional forces, ρ is the density and g is the gravitational constant (Holton and Hakim 2013).

When performing a scale analysis for the boundary layer, one obtains that the non negligible forces in Equations (2.1)-(2.3) are the pressure gradient, friction forces and Coriolis forces. Hence, the resulting equations for the PBL are (Holton and Hakim 2013)

$$\frac{Du}{Dt} - fv = -\frac{1}{\rho} \frac{\partial p}{\partial x} + F_{rx}, \quad (2.5)$$

$$\frac{Dv}{Dt} + fu = -\frac{1}{\rho} \frac{\partial p}{\partial y} + F_{ry}, \quad (2.6)$$

$$\frac{Dw}{Dt} = -\frac{1}{\rho} \frac{\partial p}{\partial z} - g + F_{rz}. \quad (2.7)$$

2.1.1 The roughness sublayer

The roughness sublayer is situated at the top of the forest canopy. Inside this layer the turbulent eddies are coherent and the length scale of the eddies are of the canopy height (Dellwik, Landberg, and Jensen 2006). The coherent eddies affect the turbulent motions in the surface layer. Hence, the roughness sublayer is important for the flow around a wind turbine when a forest is present.

2.1.2 The surface layer

The surface layer is characterized by a large vertical wind-speed gradient (Emeis 2012). Inside the surface layer, the wind profile can in average be described by the logarithmic wind law, given by

$$\bar{u} = \frac{u_*}{\kappa} \ln \left(\frac{z}{z_0} \right), \quad (2.8)$$

where u_* is the friction velocity, κ is the von Kármán constant ($\kappa \approx 0.4$), \bar{u} is the mean wind-speed, z is the height above ground level (AGL) and z_0 is the roughness length. The surface layer covers the lowest 10% of the PBL, which is why its characteristics are most influential for the flow around wind turbines.

2.1.3 The Ekman layer

The wind direction inside the Ekman layer is determined by the pressure gradient force, the Coriolis force and the frictional force. Hence, one gets the following balance equation for the horizontal velocity

$$\begin{aligned} F_{rx} + f(v - v_g) &= 0, \\ F_{ry} - f(u - u_g) &= 0. \end{aligned}$$

where u_g, v_g are the geostrophic wind components in the horizontal direction. The main feature of the Ekman layer is the spiraling velocity field. Close to the ground the frictional forces are large. As one moves away from the ground the wind field turns away from the lower pressure, resulting in a spiraling motion, ending in the direction parallel to the isobars (Holton and Hakim 2013).

2.1.4 The geostrophic wind

Above the PBL, the horizontal wind is described by a balance between the pressure gradient and Coriolis force referred to as the geostrophic wind (Emeis 2012). Hence, Equations (2.1) and (2.2) reduce to

$$\begin{aligned} -fu &= \frac{1}{\rho} \frac{\partial p}{\partial y}, \\ fv &= \frac{1}{\rho} \frac{\partial p}{\partial x}. \end{aligned}$$

Occasionally, in stable atmospheric conditions, the geostrophic wind may affect the wind-power production. Though the surface layer and Ekman layer are of more importance since it contributes more to the effects of the wind flow around a wind turbine.

2.1.5 Atmospheric stability

The atmosphere can be divided into three different stability classes (Petersen et al. 1997):

- Unstable – the warm surface is heating the atmosphere and vertical mixing is increased.
- Neutral – the surface is neither heating nor cooling the air and the turbulence is generated mechanically by wind shear.
- Stable – the surface is cooling the atmosphere, which dampens vertical mixing.

2.1.6 Weibull distribution

It has been shown that, for moderate to high wind speeds, the wind resource is distributed according to the Weibull distribution function (Petersen et al. 1997). The Weibull distributions were the main idea behind the European Wind Atlas (Troen and Lundtang Petersen 1989), which later were developed into the WASP software. The Weibull distribution can be described by two parameters, the scale parameter (A m/s) and the shape parameter (K) (Petersen et al. 1997).

$$W(x, A, K) = \left(\frac{K}{A}\right) \left(\frac{x}{A}\right)^{K-1} e^{-\left(\frac{x}{A}\right)^K} \quad (2.9)$$

where x is the horizontal wind speed. The scale parameter (A) is often proportional to the mean wind speed of the distribution (Emeis 2012). The shape parameter describes the shape of the distribution, for $K = 1$ the distribution is exponential and for $K \approx 3.4$ the distribution is almost Gaussian normal distributed (Emeis 2012).

2.2 Reynolds-averaged Navier-Stokes equations

In turbulent flows, one can divide instantaneous variables into mean and fluctuating parts (Davidson 2011), the so-called Reynolds decomposition,

$$\phi = \bar{\phi} + \phi', \quad (2.10)$$

where $\bar{\phi}$ is defined as the average over time

$$\bar{\phi} = \frac{1}{2T} \int_{-T}^T \phi(t) dt. \quad (2.11)$$

Inserting this decomposition into the Navier-Stokes equations and subsequent time averaging of all terms, yields the Reynolds-averaged Navier-Stokes (RANS) equations

$$\frac{\partial}{\partial x_j} (\rho_0 \bar{v}_i \bar{v}_j) = -\frac{\partial \bar{P}}{\partial x_i} + \mu \frac{\partial^2 \bar{v}_i}{\partial x_j \partial x_j} - \frac{\partial \tau_{ij}}{\partial x_j} - \beta \rho_0 (\bar{\theta} - \theta_0) g_i. \quad (2.12)$$

In addition to the Reynolds-averaged momentum equations the continuity equation in Reynolds-averaged form becomes

$$\frac{\partial \bar{v}_i}{\partial x_i} = 0 \quad (2.13)$$

The RANS equations describe the mean quantities of the flow (Davidson 2011) and therefore reduce the amount of required computational power. More accurate ways to model the flow are Unsteady-RANS, Large Eddy Simulation and Direct Numerical Simulation. These are more expensive in terms of required computer power.

2.3 Turbulence models

Inside the atmospheric boundary layer, almost all flows are turbulent. Turbulence behaves in an irregular and chaotic way and consists of eddies, which have different length scales (Davidson 2011). The closer one gets to the ground, the smaller the length scales of the eddies become. The largest eddies are of the same order as the boundary layer (for PBL $\approx 10^3 m$). At the smallest scales, energy is transformed from turbulent kinetic energy to thermal energy through dissipation. When the flow is turbulent, the diffusion inside the flow increases (there is a larger mixing). Turbulence occurs at high Reynolds numbers

$$Re = \frac{UL}{\nu}, \quad (2.14)$$

where U is a typical velocity, L is a typical length scale and ν is the kinematic viscosity (Davidson 2011). For the PBL the Reynolds number is of the $\mathcal{O}(10^9)$.

2.3.1 k- ε model

Here, the k- ε equations are used to model turbulence. The turbulent kinetic energy, k , is defined as

$$k = \frac{1}{2} \overline{(v'_i v'_i)} \quad (2.15)$$

and the dissipation, ε , is defined as

$$\varepsilon = \nu \overline{\frac{\partial v'_i}{\partial x_j} \frac{\partial v'_i}{\partial x_j}}. \quad (2.16)$$

From the exact k -equation one can derive the modeled k -equation (Davidson 2011). The modeled k -equation is given by

$$\frac{\partial k}{\partial t} + \bar{v}_j \frac{\partial k}{\partial x_j} = \nu_t \left(\frac{\partial \bar{v}_i}{\partial x_j} + \frac{\partial \bar{v}_j}{\partial x_i} \right) \frac{\partial \bar{v}_i}{\partial x_j} - \varepsilon + \frac{\partial}{\partial x_j} \left[\left(\nu + \frac{\nu_t}{\sigma_k} \right) \frac{\partial k}{\partial x_j} \right], \quad (2.17)$$

with

$$\nu_t = C_\mu \frac{k^2}{\varepsilon}. \quad (2.18)$$

Using Equation 2.17 together with physical reasoning one can formulate the modeled ε -equation

$$\frac{\partial \varepsilon}{\partial t} + \bar{v}_j \frac{\partial \varepsilon}{\partial x_j} = \frac{\varepsilon}{k} C_{\varepsilon 1} \nu_t \left(\frac{\partial \bar{v}_i}{\partial x_j} + \frac{\partial \bar{v}_j}{\partial x_i} \right) \frac{\partial \bar{v}_i}{\partial x_j} - C_{\varepsilon 2} \frac{\varepsilon^2}{k} + \frac{\partial}{\partial x_j} \left[\left(\nu + \frac{\nu_t}{\sigma_\varepsilon} \right) \frac{\partial \varepsilon}{\partial x_j} \right]. \quad (2.19)$$

	$C_{\varepsilon 1}$	$C_{\varepsilon 2}$	C_μ	σ_k	σ_ε
Standard	1.440	1.920	0.090	1.000	1.300
Modified	1.440	2.223	0.030	1.000	1.300

Table 2.1: Empirical constants in the k- ε model. The modified constants are tuned for an atmospheric flow (Mandas et al. 2004).

All constants in the k- ε equations are determined through experiments and the standard and modified atmospheric values are given in Table 2.1.

2.3.2 Turbulence intensity

The turbulent intensity (TI) is a measure of how turbulent the flow is. The turbulent intensity usually varies between 10 – 30% and is large over forests

$$TI = \frac{\sqrt{k}}{|\mathbf{U}|}. \quad (2.20)$$

For a flat-plate boundary layer, one can approximate the TI at a certain height with the help of the roughness length (z_0) (Petersen et al. 1997)

$$TI \approx \frac{1}{\ln \left(\frac{z}{z_0} \right)}. \quad (2.21)$$

3 Method

The wind farm is located just outside of Dingle on the west coast of Sweden embedded in a hilly and forested landscape. The geographic location can be seen in Figure 3.1. The wind farm is planned to consist of 13 wind turbines with a total height of 150 m AGL. Inside the wind farm three different measurement locations have been used (see Figure 3.2).

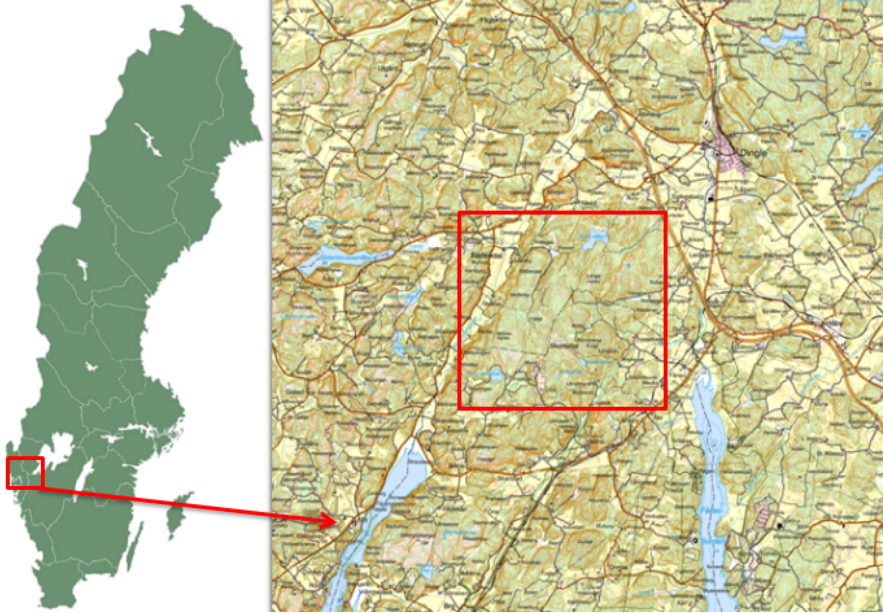


Figure 3.1: *The geographical location of Skottfjället where the wind farm is located. The terrain map is extracted from the Sveriges Lantbruk Universitet (SLU) database (SLU 2015a). The red rectangle marks the zoom up figure 3.2.*

All turbine and measurement coordinates are given in Table 3.1. The vegetation at the wind farm is mainly fir trees, with an average height of 20 m above ground level (SLU 2015b).

	x [m]	y [m]	z (above sea level (ASL)) [m]
SODAR BRN	1250269	6493559	126
SODAR WWH	1249082	6493046	112
Met Mast	1249210	6492005	130
Turbine T4	1249377	6492801	130
Turbine T7	1249033	6493643	110
Turbine T8	1249279	6493444	120
Turbine T9	1249587	6493330	120
Turbine T11	1249636	6493864	120
Turbine T12	1249998	6493908	110
Turbine T13	1250223	6493598	123
Turbine T14	1250420	6494175	119
Turbine T15	1250738	6493990	110
Turbine T16	1251217	6494232	100
Turbine T17	1250963	6494389	106
Turbine T18	1251490	6494082	100
Turbine T20	1251570	6494601	100

Table 3.1: Coordinates in RT90 format for the two SODAR measurement sites and the 13 turbines used in this report.

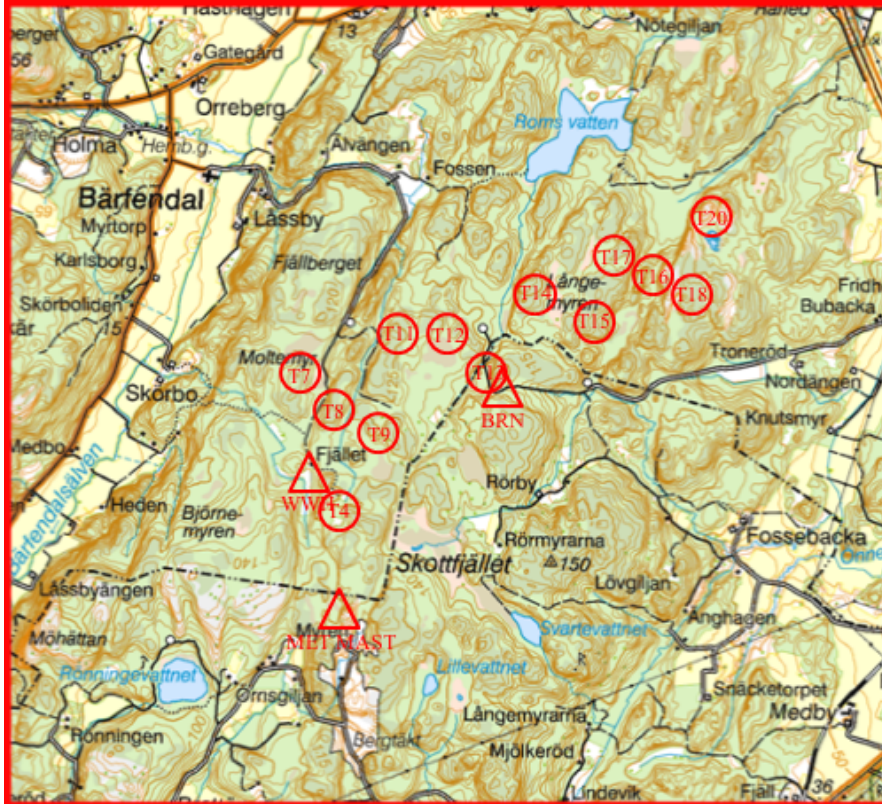


Figure 3.2: Zoomed up figure of Skottfjället including the wind farm layout. Red circles represent wind turbines and red triangles indicate measurement sites.

3.1 Measurements

The three measurement equipments that have been used is one meteorological mast and two SODAR AQ500 (AQSystem 2013), the placement of these measurements can be seen in Figure 3.2. The meteorological mast has two different measurement heights (40m and 60m). The length of the beam on which the wind measuring equipment was placed (see Appendix A Figure 6.3), was seven times the mast width, which is assumed to be good enough to avoid mast influence on the data. The mast was placed approximately two kilometers south of the wind farm and it used anemometers at the two different heights, to measure the wind characteristics. Unfortunately, there exists no calibration protocol and no information on what type of anemometers that were used. The measurement campaign for this meteorological mast was carried out from 2007-01-13 to 2008-03-17.

The SODAR BRN was placed approximately in the center of the wind farm during the time period 2012-11-01 to 2014-11-30. The BRN equipment was calibrated and checked regularly during the time period. The data series produced by the SODAR equipment were 10-min averages for wind speed, wind direction, temperature, pressure and turbulence intensity, among others. Data was provided for 31 different heights between 50-200 m with a spacing of 5 m.

The other SODAR, WWH, was placed in the west edge of the wind farm during the time period 2013-01-30 to 2014-01-16. It was, in the same way as BRN, calibrated and checked regularly during the time period. The WWH SODAR provides the same 10-min average outputs as BRN for the same vertical heights.

Due to the missing calibration protocol and its placement far south of the wind farm, the data from the meteorological mast are considered to be non-reliable and are therefore excluded from this study. A basic data validation has been performed for the two SODAR measurements. The time series chosen in Table 3.2 was investigated to check if the horizontal wind speed had any extreme values that were non coherent with the rest of the measurements. If extreme values were found, they were removed from the time series. For the WWH SODAR, large amounts of data were missing for heights above 120 m. Hence, data above this height have not been used for the SODAR WWH. If information was missing or was removed at one height, it was also removed from all other heights to get a coherent average values.

Three different time series were then chosen from the two SODARs and are presented in Table 3.2. The main time series was chosen to be BRN2013, since it had best data coverage and it had data covering a whole year taking into account all seasonal variations. The time series for BRN and WWH were chosen to be the time series, which the two SODARs had in common. In Figure 3.3, the wind distribution at 100 m for the different time series are compared with a Weibull distribution.

SODAR	Time series
BRN2013	2013-01-01 - 2014-01-01
BRN	2013-01-30 - 2014-01-16
WWH	2013-01-30 - 2014-01-16

Table 3.2: Shows names of the different time series for the SODAR measurements used in this study.

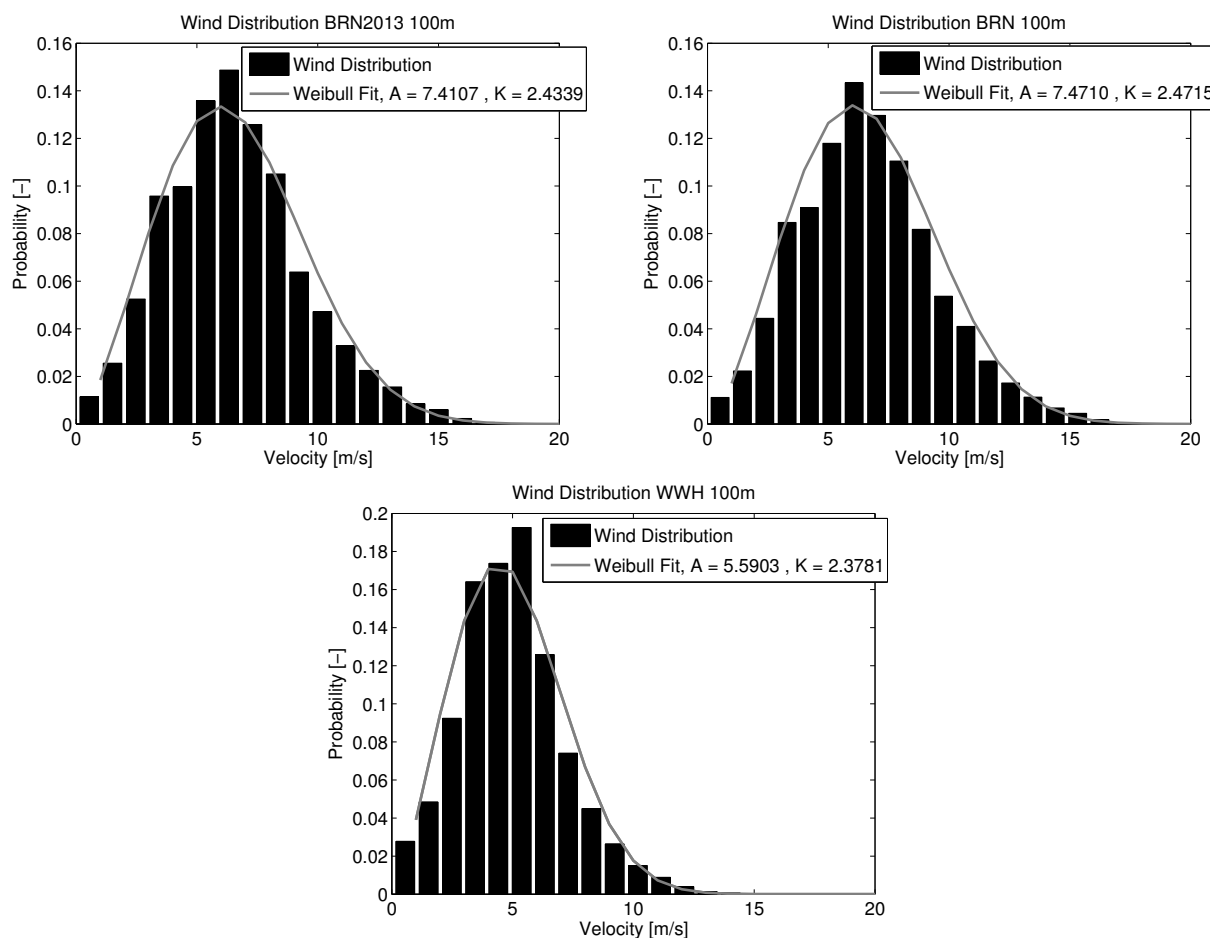


Figure 3.3: Wind distributions at 100 m for the SODAR time series of BRN2013, BRN and WWH.

3.2 OpenWind

3.2.1 Set-up

OpenWind supports geographical information system (GIS) data files. Vector "shape" files (Lantmäteriet 2013), covering the area in Figure 3.1, have been collected from the SLU database (SLU 2015a). The height contours are given with 10 m difference and are used in OpenWind to create an elevation map. The shape files also include contours enclosing landscape types e.g. open farmland, forest, buildings, water areas and moist areas.

The shape file is used to create two roughness maps of the surface according to Table 3.3. To calculate the mean wind field in OpenWind, one uses a wind map as described below. In addition to two different roughness maps, a displacement height of 20 m was used to simulate the forest. The displacement of the wind profile had to be adjusted manually. Firstly, the mean wind speed was extracted for 40, 60, 80, 100, 120 m and the wind speed at these heights was adjusted 20 m upward (40 m mean wind speed became the 60 m mean wind speed etc). Secondly, the wind profile was shifted to match the 100 m wind speed of the SODAR.

	Roughness map 1	Roughness map 2
Units	z_0 [m]	z_0 [m]
Forest	0.5	2
Building	0.5	2
Open Farmland	0.03	0.03
Water Area	0.001	0.001
Moist Area	0.001	0.001

Table 3.3: Roughness length, z_0 [m]. For the forests and buildings two different roughness lengths were used (Dellwik, Arnqvist, et al. 2014), resulting in two roughness maps.

3.2.2 Creating a windmap

OpenWind is based on the NOABL code (Phillips and Traci 1979), which generates a three-dimensional divergence-free wind field. This wind map reads the elevation, roughness and SODAR measurement and creates a wind map for 12 different directions covering 360° for six different output heights. Firstly, the wind field is initialized using a interpolation-extrapolation scheme (Phillips and Traci 1979). The scheme accounts for the roughness, elevation, atmospheric stability and observational data from a SODAR or a meteorological mast. The observational data is extrapolated in the vertical direction and the extrapolation assumes a power law, which can be compared with the logarithmic wind law (see Section 2.1.2).

$$|\vec{v}|_m = |\vec{v}|_0 \left(\frac{z_m}{z_0} \right)^\beta, \quad (3.1)$$

$$u_m = -|\vec{v}|_m \sin(\theta), \quad (3.2)$$

$$v_m = -|\vec{v}|_m \cos(\theta), \quad (3.3)$$

where $|\vec{v}|_m$ is the observed absolute velocity at the measurement height, z_m , $|\vec{v}|_0$ is the wind speed at height z_0 , previously defined as the friction velocity u_* , β is the wind-shear exponent adjusted to neutral stability conditions (often chosen to be 0.14 (Petersen et al. 1997)) and θ is the direction of the wind. In Equation (3.1) the friction velocity is calculated from the observational data of the measurements, which is subsequently used to calculate the velocity at the top of the atmospheric boundary layer (in OpenWind the top of the atmospheric boundary layer is defined to be 200 m AGL). OpenWind then uses Equations (3.1) - (3.3), but replaces the measurement height with the atmospheric boundary layer height. The horizontal wind components at 200 m height AGL are then spread horizontally to all other nodes. For each horizontal node at 200 m, Equation (3.1) is used to determine the friction velocity below that node (Phillips and Traci 1979). With each new friction velocity the velocity components at all node heights can be calculated according to Equations (3.1) - (3.3). After this calculation is completed, every node in the domain has two horizontal velocity components. The vertical wind component is initially set to zero.

In the next step, the model is iterated for each wind direction, trying to create a divergence-free wind field (Phillips and Traci 1979). Assuming that the initial wind field is given by (u_i, v_i, w_i) the divergence-free wind field can be written as,

$$u = u_i + u', \quad (3.4)$$

$$v = v_i + v', \quad (3.5)$$

$$w = w_i + w'. \quad (3.6)$$

where $(')$ represents a correction term defined as,

$$u' = \tau_h \frac{\partial \phi}{\partial x}, \quad (3.7)$$

$$v' = \tau_h \frac{\partial \phi}{\partial y}, \quad (3.8)$$

$$w' = \tau_v \frac{\partial \phi}{\partial z}. \quad (3.9)$$

where ϕ is the perturbation velocity potential. It describes the initial error in the wind field and is adjusted for terrain influences (Phillips and Traci 1979). τ_h and τ_v are constants that model the deviation of the atmosphere from neutral conditions (Phillips and Traci 1979). In order to calculate the perturbation velocity potential the continuity equation for the divergence-free velocity field is used (Phillips and Traci 1979). It reads

$$\frac{\partial u}{\partial x} + \frac{\partial v}{\partial y} + \frac{\partial w}{\partial z} = 0 \quad (3.10)$$

$$\frac{\partial u'}{\partial x} + \frac{\partial v'}{\partial y} + \frac{\partial w'}{\partial z} = -\frac{\partial u_i}{\partial x} - \frac{\partial v_i}{\partial y} - \frac{\partial w_i}{\partial z} \quad (3.11)$$

$$\frac{\partial}{\partial x} \left(\tau_h \frac{\partial \phi}{\partial x} \right) + \frac{\partial}{\partial y} \left(\tau_h \frac{\partial \phi}{\partial y} \right) + \frac{\partial}{\partial z} \left(\tau_v \frac{\partial \phi}{\partial z} \right) = -\frac{\partial u_i}{\partial x} - \frac{\partial v_i}{\partial y} - \frac{\partial w_i}{\partial z}. \quad (3.12)$$

By iterating this elliptic equation with correct boundary conditions the perturbation velocity potential can be computed. At solid boundaries, a zero-gradient boundary conditions is employed, while for all other boundaries, the potential is set to zero (Phillips and Traci 1979). Once the wind field has converged for all wind directions, the windmap can be used to optimize the wind-site layout, to calculate the energy production and extract the wind speed profiles.

3.2.3 Calculating the annual energy production

In OpenWind, the annual energy production (AEP) for a wind site is calculated as (Truepower 2010)

$$AEP = 8766 \sum_{i=1}^{nD} \sum_{j=1}^{nU} \sum_{k=1}^{nT} F_{ijk} P_{ijk} \quad (3.13)$$

where 8766 is the average number of hours in one year, nD is the number of direction steps, nU is the number of wind speed steps, nT is the number of wind turbines, F_{ijk} is the probability that the wind comes from direction i with wind speed j at turbine k , P_{ijk} is the power generated by the turbine k for a given wind direction i and wind speed j . The wind speeds j ranges from 1 – 30 m/s with a 1 m/s bin size. F_{ijk} can also be described as a wind distribution map. In order to calculate the probability F_{ijk} , one needs a windmap and access to a observational data with wind speed and wind direction data.

In this report, the AEP is calculated for the Vestas V90 2MW wind turbine. The power and trust values for the wind turbine are displayed in Table 3.4. The wake effect model has been chosen to be a modified park model (Truepower 2010) with at constant wake decay of 0.075.

3.3 STARCCM+

3.3.1 Set-up

In STARCCM+, the simulations are given a reference inlet velocity at a reference height and are solved for one wind direction at a time. The wind directions are chosen to be the same as in OpenWind (12 directions with 30° sectors covering 360°). The terrain elevation and roughness length (Table 3.3) are imported from OpenWind. According to the wind park siting manual (CD-Adapco 2010), it is recommended to have a 3 – 5 km buffer zone around the wind farm to avoid boundary effects. In order to save computational time, the

Wind Speed [m/s]	Power [KW]	C_t [-]
4	89	0.838
5	203	0.808
6	363	0.804
7	591	0.807
8	884	0.784
9	1224	0.717
10	1583	0.628
11	1876	0.525
12	1980	0.402
13	1998	0.306
14	2000	0.239
15	2000	0.192
16	2000	0.157
17	2000	0.131
18	2000	0.110
19	2000	0.094
20	2000	0.081
21	2000	0.070
22	2000	0.062
23	2000	0.054
24	2000	0.048
25	2000	0.043

Table 3.4: Power and thrust curves for Vestas V90 2MW. Hub height 105 m and rotor diameter 45 m. Power and thrust values are given for a constant density of 1.225 kg/m³. The cut-in wind speed is 4 m/s and the cut-off wind speed is 25 m/s (Vestas 2010).

terrain extracted from the SLU database (see Figure 3.1) is cropped to a 5 km buffer zone. The resulting domain becomes approximately 12×12 km² in the horizontal direction.

For the meshing, a trimmer mesh was used with refinements close to the ground, as well as around wind turbine and SODAR locations (see Figure 3.4). The flow is solved using RANS with a k - ϵ closure model (see Section 2.2 and 2.3.1) with constants according to the modified values in Table 2.1. The k - ϵ turbulence model is chosen since it is a well studied model that is easy to implement. The forest is modeled with a canopy model, which adds source terms (CD-Adapco 2010) to the momentum, k and ϵ equations (Equations (2.12),(2.17),(2.19) respectively)

$$Sf_{\text{mom}} = 0.5\rho\alpha C_D|U|U_i, \quad (3.14)$$

$$Sf_k = 0.5\rho\alpha C_D|U|^3, \quad (3.15)$$

$$Sf_\epsilon = 0.5\frac{\epsilon}{k}C_{\epsilon 4}\rho\alpha C_D|U|^3, \quad (3.16)$$

where $\alpha = 0.08$ is the leaf foliage area per unit volume, $\rho = 1.225$ is the density, $C_D = 0.2$ is the canopy drag coefficient and $C_{\epsilon 4} = -0.33$ is a constant in the ϵ -equation.

The domain is a rectangular box and includes six different boundaries: Ground, Sky, North, South, West and East. The sky (at 10000 m) is set to be a frictionless, rigid lid and the ground is treated as a rough wall. Depending on the chosen wind direction, the inlet is set as a velocity inlet and the outlet is set as a pressure outlet. At the inlet boundary, a logarithmic wind speed profile is prescribed as

$$u_{log} = \frac{u_*}{\kappa} \log\left(\frac{z_h + z_0}{z_0}\right), \quad (3.17)$$

with u_* being the friction velocity derived from the reference wind speed at the reference height given in Table 3.5 and z_h being the height above ground.

Sector [°]	Wind Speed [m/s]	Occurrences [%]
345-15	5.5	16.0
15-45	5.5	20.1
45-75	6.5	19.3
75-105	6.5	19.9
105-135	5.5	19.5
135-165	6.5	19.0
165-195	6.5	16.0
195-225	6.5	15.3
225-255	8.5	15.0
255-285	7.5	11.2
285-315	5.5	14.4
315-345	6.5	13.4

Table 3.5: Reference velocity at 100 m, 1 m/s bin size and for 12 different sectors. Data was extracted from SODAR BRN in the period 2013-01-01 – 2014-01-01. The occurrences are based on the total number of times the SODAR registered a wind speed inside each 30° sector.

The inlet wind-speed profile is then split into the horizontal directions as

$$\vec{v}_{inlet} = (u_{log} \cos(\theta), u_{log} \sin(\theta), 0). \quad (3.18)$$

where θ is the wind direction specified in the simulation. This calculation gives a horizontal inlet wind speed according to the logarithmic wind profile (see Section 2.1.2). Above 1000 m the velocity inlet boundary condition is set to a constant wind speed.

Every wind direction is ran for 800 iterations, after which the simulation has converged. In Figure 3.5, an example of the wind field after 800 iterations is shown.

Wind turbines are simulated through a virtual disk in STARCCM+. The virtual disk uses 1D momentum theory to simulate the wake effect generated by the turbine. The 1D momentum method simulates the wake by adding a source term to the momentum equation, accounting for tangential and axial forces (CD-Adapco 2012). Parameter settings for the virtual disk can be found in Appendix Table 6.3.

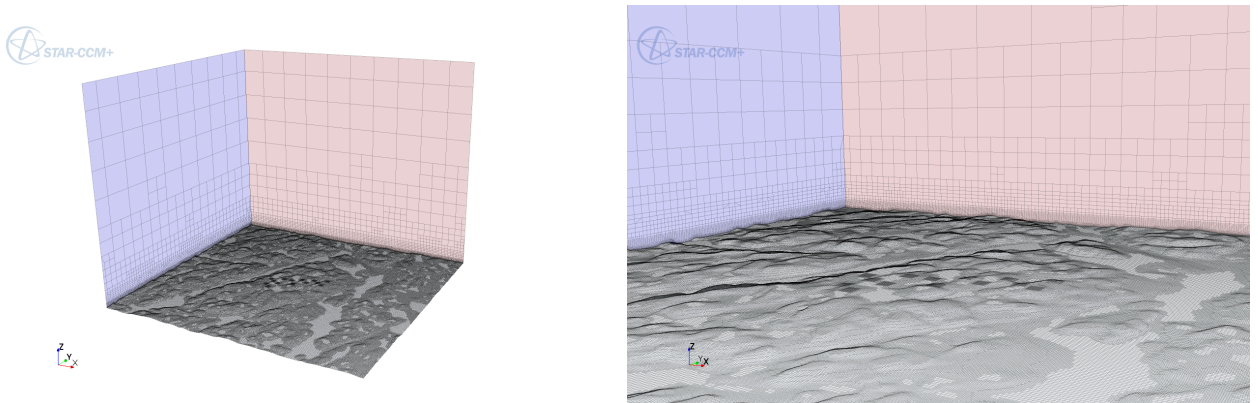


Figure 3.4: *Terrain and mesh for STARCCM+.*

3.3.2 Calculating the mean free velocity

In order to calculate the mean free velocity from the simulation result, probes are placed within the domain at the locations and heights of interest. The magnitude of the horizontal wind speed is extracted from these probes. The result of the probes is then correlated with the magnitude of the horizontal wind speed at the

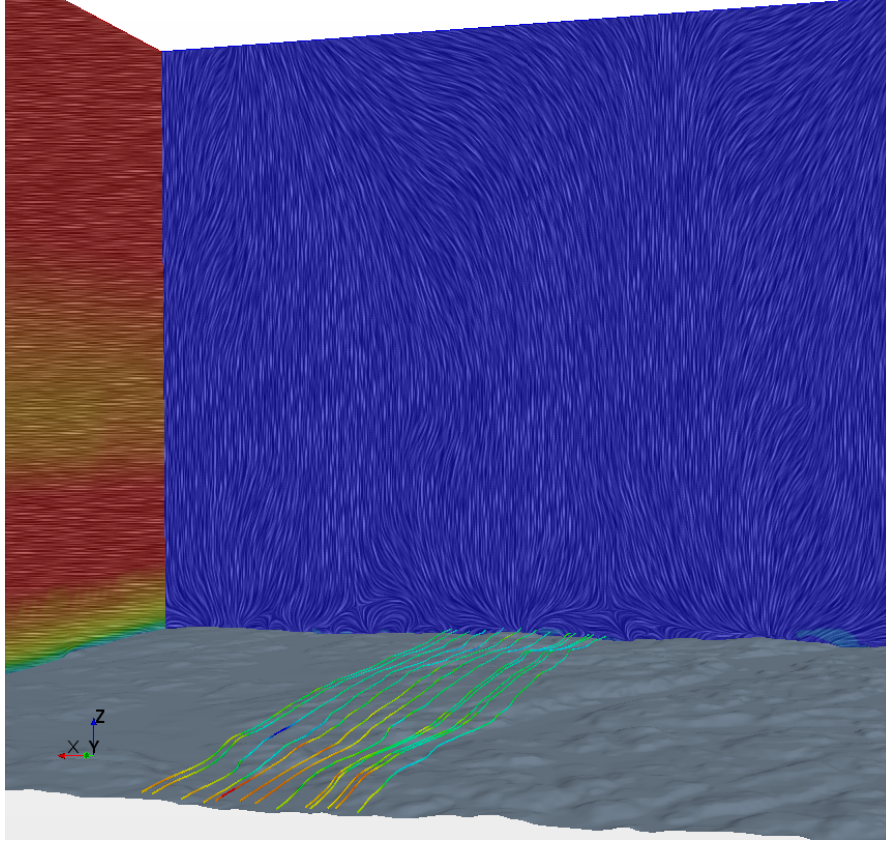


Figure 3.5: *Example of the wind flow for 0° wind direction after 800 iterations. The left boundary is the east boundary and the downstream boundary is the south boundary. These boundaries show the vector field in the north to south direction. Velocity streamlines are shown passing through the wind turbines. The wind turbines are placed in the center of the domain although they are not visible.*

measurement location, inside the simulation, using speed-up factors

$$\text{SpeedUpFactor} = \frac{V_{\text{sim}}(\text{Probe})}{V_{\text{sim}}(\text{SODAR100m})}. \quad (3.19)$$

Hence, the ratio between the horizontal wind speed at the probe location and the horizontal wind speed at the location of the SODAR at 100 m height inside the simulation, gives the speed-up factor. These speed-up factors are calculated for all probes and for all 12 directions. Each of these speed-up factors are then weighted with the probability that the wind is coming from that direction.

$$\text{SpeedUpFactorAllDir} = \text{SpeedUpFactor000Prob000} + \text{SpeedUpFactor030Prob030}... \quad (3.20)$$

The probability for each direction is extracted from the observational data (Table 3.6). With the weighted speed up factor, the velocity at the probe location can then be calculated as

$$\text{MeanWindSpeed}(\text{Probe}) = \text{SpeedUpFactorAllDirections} \cdot \text{MeanWindSpeed}(\text{SODAR100m}) \quad (3.21)$$

3.3.3 Calculating the annual energy production

The annual energy production is estimated using the power curve from Table 3.4 and the wind distribution data from the measurements and is given for one wind turbine by

$$AEP = 8766 \sum_{ij} P(SU_{ref} v_i) F(v_i, \theta_j), \quad (3.22)$$

Sector [°]	BRN2013	BRN	WWH
345-15	0.0353	0.0368	0.0368
15-45	0.0538	0.0459	0.0514
45-75	0.1002	0.0866	0.0894
75-105	0.0980	0.0986	0.1087
105-135	0.0596	0.0623	0.0615
135-165	0.0623	0.0665	0.0677
165-195	0.0777	0.0811	0.0920
195-225	0.1419	0.1443	0.1378
225-255	0.1705	0.1747	0.1515
255-285	0.1123	0.1135	0.1139
285-315	0.0442	0.0440	0.0421
315-345	0.0442	0.0458	0.0474

Table 3.6: The probability that the wind is coming from a certain wind direction for BRN2013, BRN and WWH time series.

where SU_{ref} is the speed-up factor, P is the power curve of the wind turbine and F is the measured wind distribution map. The measurement data at a height of 100 m have good data coverage in both SODARs and are chosen to represent the hub height of the wind turbines.

3.4 WRF

WRF is a mesoscale NWP model. The simulations were carried out by WeatherTech in Uppsala. The WRF model has two different dynamical solvers: the advanced research WRF (ARW) and the non-hydrostatic Mesoscale Model (NMM). In this study the ARW solver has been used. The WRF model solves a compressible form of the Euler equations, which are non-hydrostatic and conservative for scalar variables (Skamarock et al. 2005). WRF consists of different schemes to handle for example micro-physics, planetary boundary layer and surface physics etc. All schemes and descriptions can be found in technical description of the model (Skamarock et al. 2005). The model uses, in this experiment, five nested meshes, where the outer domain has a grid resolution of 27×27 km² and the resolution increases with a factor three in each nesting level; the innermost nest has a model grid resolution of 333×333 m². Further, it has 41 vertical levels, with 10 equally spaced vertical levels in the lowest 250 m. The period 2013-01-01 – 2014-01-01 was simulated using ERA Interim as initial and lateral boundary conditions. ERA Interim is a re-analysis dataset provided by European Center for Medium-range Weather Forecasts (ECMWF). The model gives hourly output of wind speed, wind direction, pressure, temperature and relative humidity. Six different heights (40, 60, 80, 100, 120, 140 m) AGL were extracted, assuming a displacement height for the forest of 15 m, for the locations of the SODARs and the wind turbines according to Table 3.1.

3.5 WindPRO

When performing a production estimation for the wind farm, OpenWind and STARCCM+ are compared with an old consultant report in WindPRO. This simulation used the meteorological mast and the Vestas wind turbine, described in Table 3.4, as input. The WindPRO results uses a simple Park wake model with a constant wake decay of 0.075. The WindPRO software have many similarities with OpenWind and is frequently used in siting simulations. In annual energy production estimations both STARCCM+ and OpenWind are adjusted to have as similar settings as possible compared with the WindPRO result.

3.6 Limitations

In order to get as accurate predictions as possible, it is important to be aware of each of the model's limitations. For OpenWind an analysis was performed for different mesh sizes. The two different meshes used in this analysis were equidistant grids with resolutions of 25 m and 50 m. The test cases were carried out with a displacement

of 20 m and roughness map 2 according to Table 3.3. The same test was carried out for STARCCM+, where the cell count for the coarse mesh was 2.7×10^6 and for the fine mesh 4.2×10^6 . The result of these comparisons is shown in Figure 3.6. In OpenWind, the result is identical between the two meshes. For STARCCM+, there is a minimal difference at 140 m and 60 m. In STARCCM+, the inlet boundary condition is set according to a reference velocity which is chosen by the user. Different reference velocities have been tested: in the first case, a constant reference velocity of 6.2 m/s was chosen for all directions and for the second case, the reference velocity was set according to Table 3.5. The error between the speed-up factors of the two cases was found to be of $\mathcal{O}(10^{-6})$. Furthermore, it is possible to define a reference turbulent intensity at the reference height in STARCCM+. This turbulent intensity was chosen to be a constant value of 13% for all wind direction, due to that measurement of the turbulent intensity in STARCCM+ has been shown to be non-accurate (Tomkins 2007).

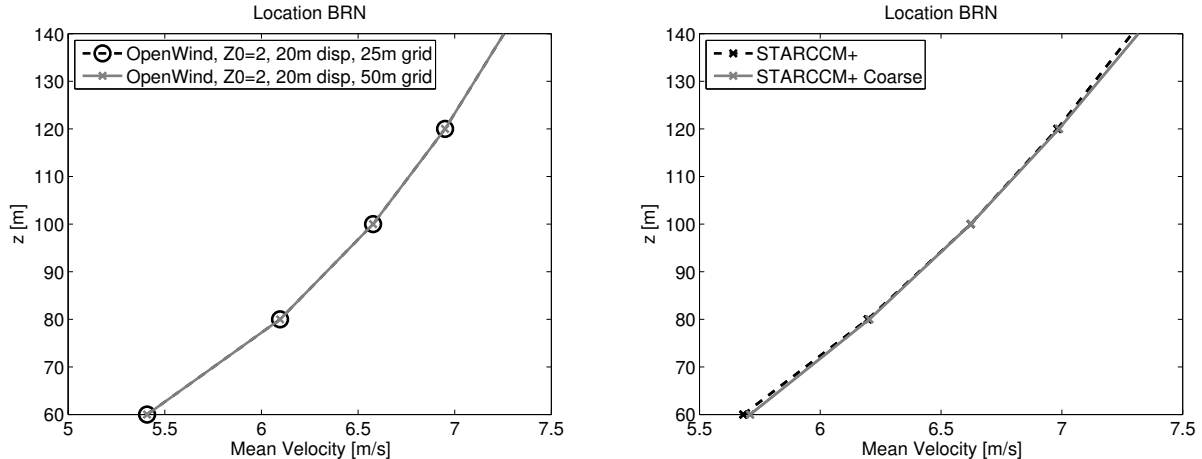


Figure 3.6: Comparison of the wind profiles for different cell sizes. The left panel shows the result using OpenWind and the right panel shows the result using STARCCM+.

Both OpenWind and STARCCM+ are dependent on the observational data. Hence, it is of great importance that these data are accurate and can be trusted. In Section 3.1 a basic validation for the SODAR measurements was performed and the equipment was calibrated regularly during the measurement campaign. The SODAR WWH had to be moved three times due to disturbance of forestry machinery before a satisfying location without disturbances was found. This location was in a valley with surrounding hills (see Appendix Figure 6.1). This explains the low wind speeds for SODAR WWH close to the ground and makes prediction hard, since good elevation data together with good horizontal resolution in the models are needed to capture this effect. More pictures of the installation of SODARs and meteorological mast can be found in Appendix.

OpenWind is based on simple equations and includes many simplifications to calculate the wind resource. STARCCM+ solves full flow equations and models turbulence to calculate the wind resource. Since the WRF model runs were performed by WeatherTech, tests of different mesh sizes and boundary conditions were not possible. The horizontal resolution of the WRF is coarse and the model is totally independent of measurements inside the wind farm.

With OpenWind and STARCCM+ the simulations were limited in order to be run on a single computer. The computational demand for the different simulation tools is summarized in Table 3.7

Model	Time scale
OpenWind	Hours
STARCCM+	Days
WRF	Weeks

Table 3.7: Computational demand for the three models.

4 Result and discussion

4.1 Model comparison

To compare the different models, the mean wind speed profiles have been used as analyzing tool. By investigating the mean wind speed profiles, one uses the raw format of the models and additional uncertainties, concerning wind turbine information are removed from the predictions. The results presented in Figure 4.1 and 4.2 are used to determine the most accurate setting for OpenWind and STARCCM+.

In order to investigate which roughness map that worked best in OpenWind and STARCCM+ both models were ran with both roughness maps (Table 3.3). The mean wind speed profiles obtained with the different roughness maps are compared with the observational data of SODAR BRN2013 in Figure 4.1 and 4.2. For OpenWind an additional test with roughness map 2 was performed with a displacement height of 20 m.

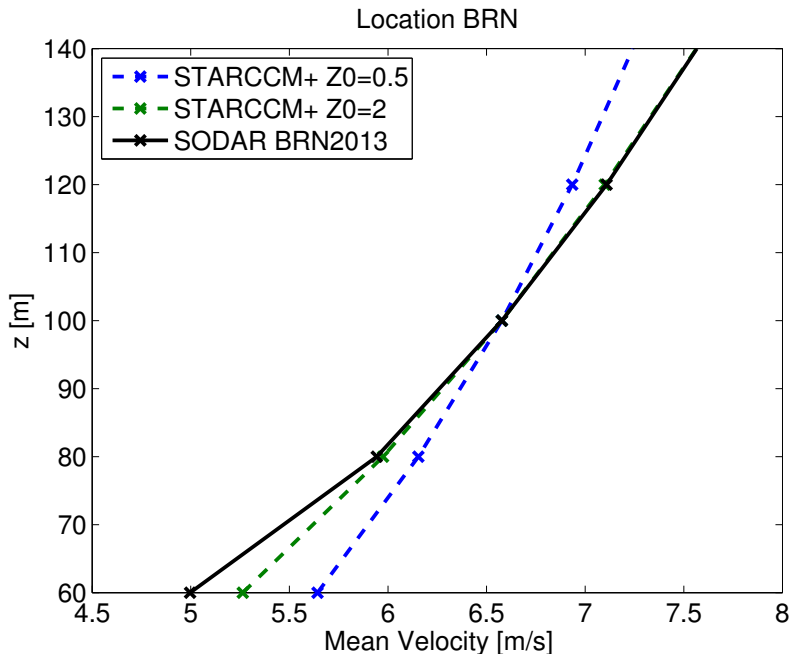


Figure 4.1: Comparison of the simulated wind profiles in STARCCM+ using two different roughness lengths for the forest and buildings. The wind profiles for STARCCM+ are calculated with the measurement from the SODAR BRN2013 at the BRN location.

The most accurate result, compared to the observational data, is found for roughness map 2 with increased z_0 for forests and buildings. This result indicates that $z_0 = 0.5$ m is not enough to calculate the wind shear observed above this forest. Hence, roughness map 2 will be used for OpenWind and STARCCM+ from here on. In Ryningsnäs, on the east coast of Sweden, Swedish researchers have made a similar study of wind conditions above a forest (Dellwik, Arnqvist, et al. 2014). They also showed that $z_0 = 2$ m captured the actual wind shear best. Adding a displacement height of 20 m to OpenWind resulted in an even better agreement of the wind profile with the measurements.

The best simulation results from STARCCM+ and Openwind were then compared with the velocity profile of the WRF model together with observational data of the SODAR BRN2013 in Figure 4.3. Both OpenWind and STARCCM+ uses SODAR BRN2013 mean wind-speed at 100 m to compute the wind profile and that is why the mean velocities are matching exactly at 100 m. Since the WRF model was run by WeatherTech, different settings were not possible to try out. Therefore, the result given by WeatherTech are assumed to have the best possible settings. Looking at the wind profile of STARCCM+, there is only an absolute error between the prediction and observation for the values at 60 and 80 meters. For OpenWind, the wind shear should be higher in order to fit the observational data. The WRF model over-predicts the mean wind speeds at all height levels although it captures the wind shear accurately.

The root mean square error (RMSE) (see Appendix Equation (6.1)) are used to compare which model that

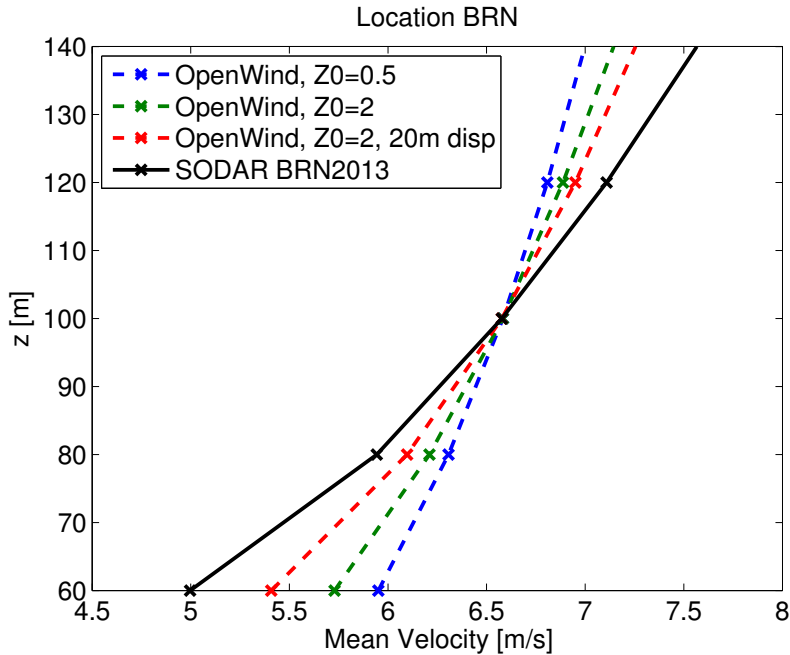


Figure 4.2: Comparison of the simulated wind profiles in OpenWind using two different roughness lengths for the forest and buildings. The profiles are calculated with the measurement from the SODAR BRN2013 at the BRN location.

is most accurate compared to the observational measurements. In Table 4.1 the RMSE show that STARCCM+ predicts the wind profile most accurately when comparing the three models. The worst accuracy is found for OpenWind, which is also the simplest model. Considering that both OpenWind and STARCCM+ are adjusted to fit the 100 m mean wind speed of the observational measurements, they have a advantage compared to the WRF model, which is only solved through boundary conditions. When only looking at the wind shear the WRF model is performing almost as good as STARCCM+.

Model	Root Mean Square Error [m/s]
OpenWind	0.28
STARCCM+	0.13
WRF	0.22

Table 4.1: The root mean square error for the wind speed profiles at the BRN location. The root mean square error for all three models are compared with the BRN2013 measurement data. The errors are calculated using the mean wind speeds at 60,80,120,140 m. The 100 m mean wind speed has not been included since OpenWind and STARCCM+ are defined through this value.

For the location of the SODAR WWH, none of the models are as accurate as for the SODAR BRN location (see Figure 4.4). The time series of the SODAR WWH and the models differ by approximately 30 days, since the models is simulated with BRN2013, but the wind conditions are assumed to not have that much difference. The STARCCM+ simulation still yields the most accurate result and for the heights of 100 and 120 m the accuracy of the model is considered to be good. OpenWind shows the second most accurate result and the WRF model shows the least accurate result. Once again, only looking at the wind shear OpenWind is the worst performing model. While the WRF model and STARCCM+ are better performing.

As mentioned above, the SODAR WWH is placed in a valley (see Section 3.6), which enplanes the low mean wind speeds at 80m and 60 m (in Figure 4.4). Since WRF has such a coarse horizontal resolution (333 m), it is not able to catch the effects of this valley (see Figure 4.5). In order to predict a hill or a valley in WRF, a resolution of at least 6-8 grid points covering the hill or valley are needed. In Figure 4.5, one can see that this is not the case for SODAR WWH (left black square) and the valley is not modeled at all. For

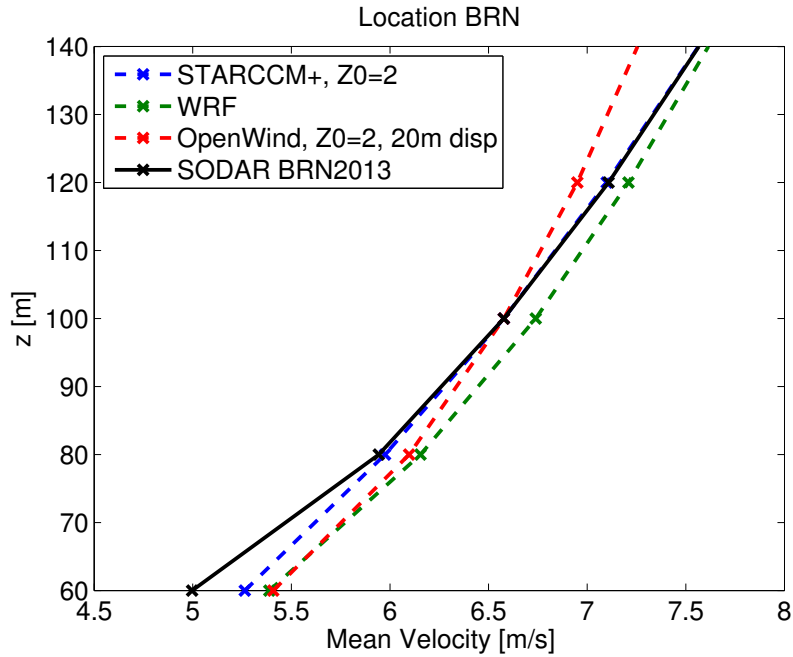


Figure 4.3: Comparison of the simulated wind profiles in STARCCM+, OpenWind, WRF with measurement data from the SODAR BRN2013 at the location of BRN.

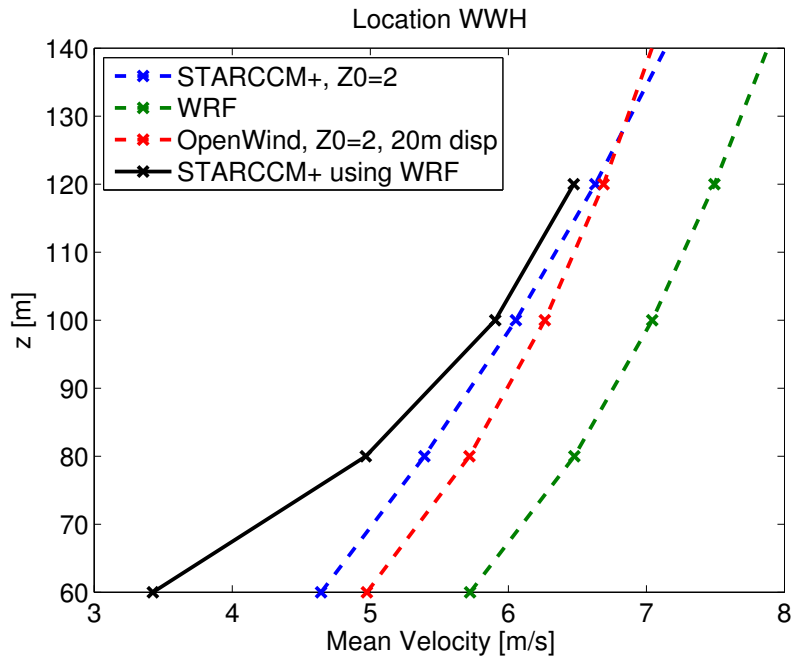


Figure 4.4: Comparison of the simulated wind profiles in STARCCM+, OpenWind, WRF with measurement data from the SODAR WWH at the location of WWH. STARCCM+ and OpenWind are simulated using BRN2013 100 m mean wind speed.

STARCCM+ and OpenWind the elevation of the terrain is determined from 10 m height contours. This terrain elevation captures the valley better, although it is not as deep as it should be.

Since the models do not predict the velocity profile of the SODAR WWH correctly, the RMSE becomes large for all models. As described above, STARCCM+ performed best and the WRF model yielded the worst prediction, which can also be seen by the RMSE in Table 4.2.

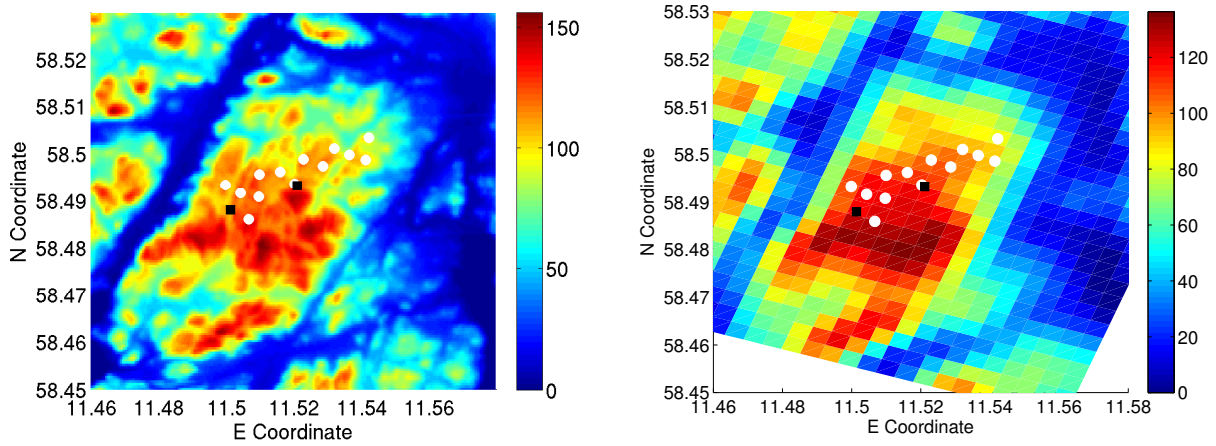


Figure 4.5: *Terrain height of Skottfjället. The left panel shows the real terrain height retrieved from Metria (Metria 2015). The right panel shows how the terrain height is simulated in the WRF model. White dots represent wind turbines and black squares represents the SODARS WWH and BRN.*

Model	Root Mean Square Error [m/s]
OpenWind	1.21
STARCCM+	1.14
WRF	1.84

Table 4.2: The root mean square error for the velocity profiles at the WWH location. The root mean square error for all three models are compared with the WWH measurement data. The errors are calculated using the mean velocities at 60,80,100,120 m.

Looking at some of the locations of the wind turbines, presented in Figure 4.6, the difference is relatively small between OpenWind and STARCCM+. The same settings, as shown in Figures 4.3 and 4.4 are used for the models. STARCCM+ is considered to give the most accurate result, compared to STARCCM+ wind speed profile, WRF shows an over-prediction except at the location of wind turbines T18 and T20. Wind turbine locations T4 and T13 represents the most common result for the wind turbines. Wind turbine locations T18 and T20 are the exceptions from the common result. At the wind turbine T18 location, the WRF model and the STARCCM+ model are almost identical while at the T20 wind turbine location WRF under-predicts the wind speed compared to STARCCM+. All of the differences is described through how the WRF model is able to predict the correct height of the terrain. At for example the wind turbine T20 location the WRF model under-predicts the terrain height and therefore predicts lower wind speeds.

The hilly landscape makes predictions using WRF hard, due to the models coarse resolution. At the BRN location, the WRF model accurately predicts the wind profile. Looking at Figure 4.5, it predicts the height for the surrounding terrain around BRN accurately. For a relatively large area with homogeneous terrain, one can expect the WRF model to successfully predict the wind profile for this location. Further, if the horizontal resolution of the WRF model was refined, one would expect to get more accurate result in non-homogeneous terrain. Since the WRF model produces time dependent results, one can use the data as input into STARCCM+ to get better horizontal resolution. This would make STARCCM+ independent of measurements.

In Figure 4.7, the models are once more compared to the SODAR WWH at the WWH location. In order to test the above assumption, STARCCM+ is ran using WRF at the BRN location as input. Here, one can see that the added horizontal resolution of using STARCCM+ together with the WRF model makes the predictions better than the normal WRF prediction and slightly more accurate than OpenWind. Hence, if this assumption was further tested a measurement campaign would not be necessary to determine the wind resource for some location.

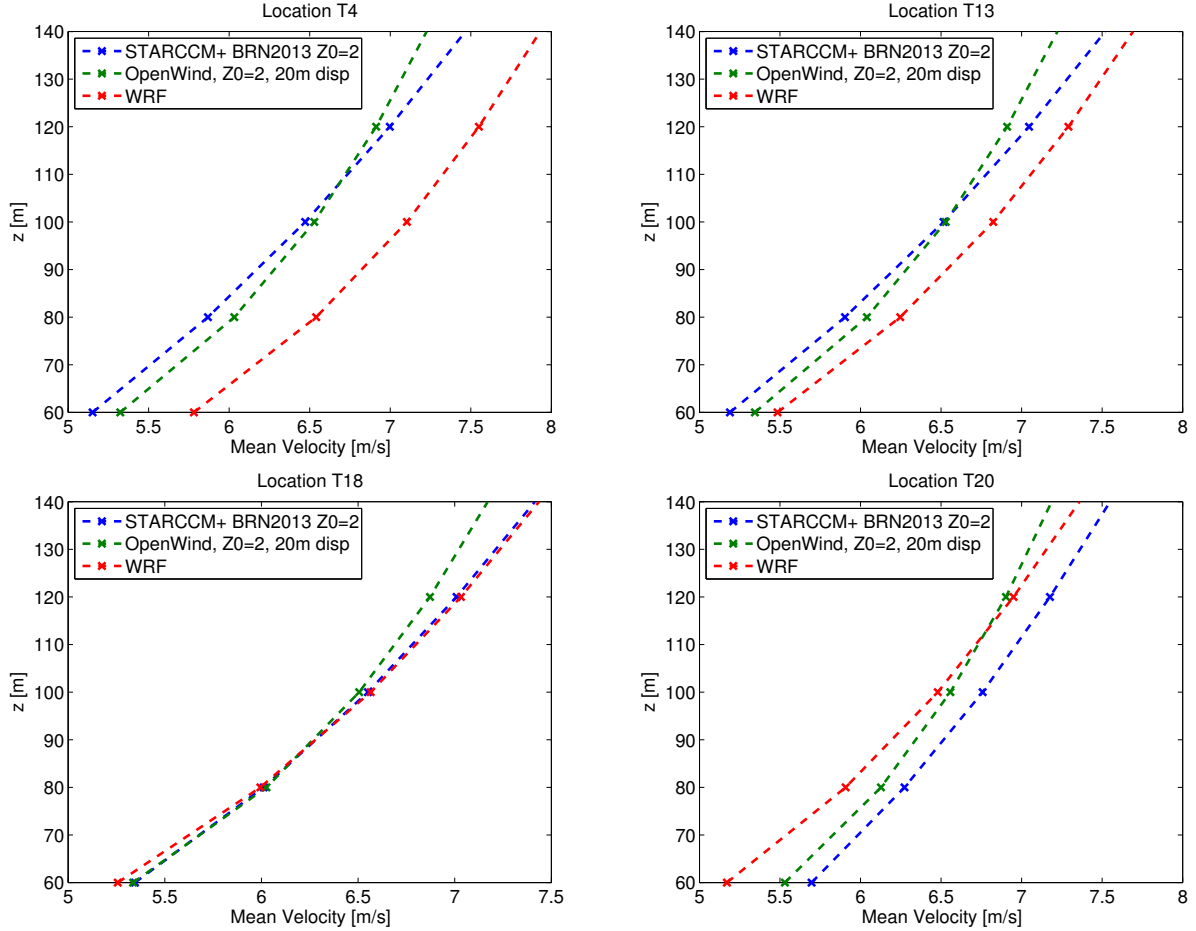


Figure 4.6: Comparison of the mean velocity profiles for four chosen wind turbine locations. Upper left panel is the location of the wind turbine T4, upper right panel is the location of the wind turbine T13, lower left panel is the location of the wind turbine T18 and lower right panel is the location of the wind turbine T20. Coordinates for these wind turbines can be found in Table 3.1 and placement inside the wind farm can be seen in Figure 3.2.

4.2 Cross prediction

To further investigate the performance of the models a cross prediction has been made in STARCCM+ and in OpenWind. The two SODARs BRN and WWH are used both with the same time series, making them comparable. Each model is given data from one SODAR as an input and the wind profiles is calculated at the other SODAR location. In STARCCM+, the wind-speed profiles are similar to the SODARs from 100 m height and upwards as shown in Figure 4.8. When using the BRN data to compute the wind-speed profile at the WWH position, the velocities are over-predicted. The opposite is true when using the WWH data to compute the wind-speed profile at the BRN location except at a height of 60 m. The absolute difference between the SODAR and its corresponding simulation result are approximately 0.3 m/s at 100 m. For OpenWind (see Figure 4.9), the wind shear is not captured correctly, the wind-speeds are over-predicted trying to simulate WWH and under-predicted when trying to simulate BRN. Furthermore, the variations in the mean wind-speeds between the SODARs are small at 100 m in OpenWind. This makes the prediction using OpenWind non-reliable in this type of forested and hilly terrain.

4.3 Production estimation

Finally, as a last evaluation of the models, the annual energy production has been compared. The annual production of each wind turbine is shown in Table 4.3. The results show that the model predictions vary between the wind turbines. STARCCM+, OpenWind and WindPRO are using the Vestas turbine described in

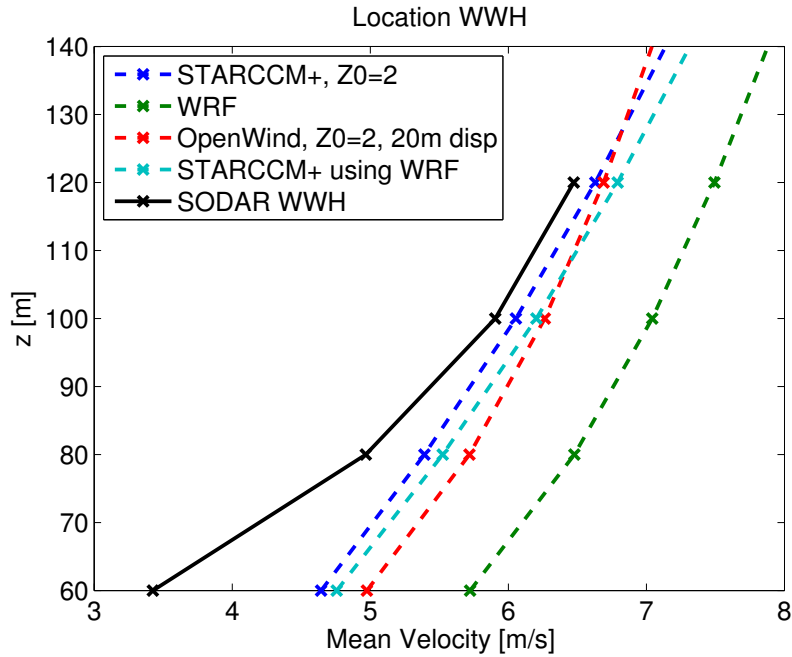


Figure 4.7: Comparison of the simulated wind profiles in STARCCM+, OpenWind, WRF and STARCCM+ using WRF as input, with measurement data from the SODAR WWH at the location of WWH.

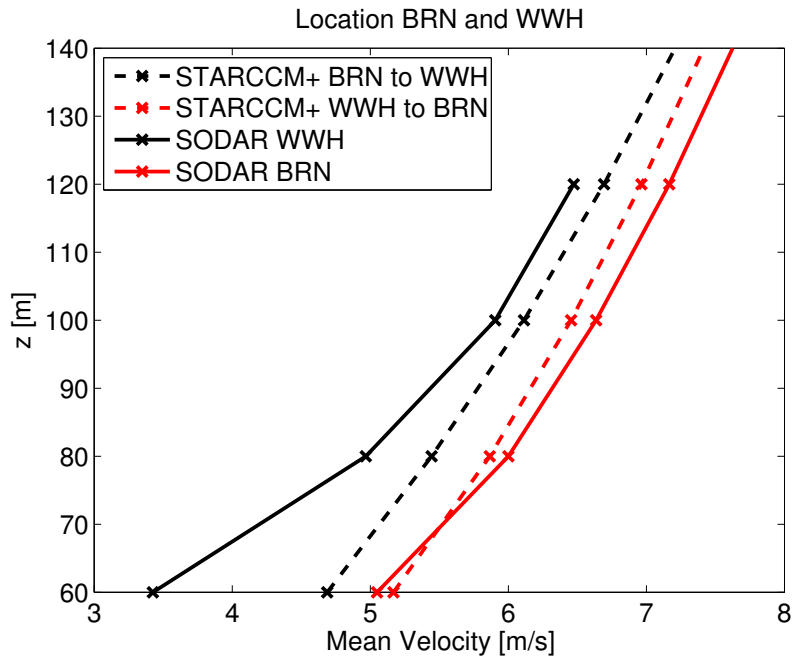


Figure 4.8: Cross prediction in STARCCM+. Wind profiles are simulated from SODAR WWH to SODAR BRN and from SODAR BRN to SODAR WWH.

Table 3.4. The wind distribution data are given from BRN2013 and roughness map 2 (Table 3.3) is used in the simulations. WindPRO uses the meteorological mast to determine the annual energy production. Looking at the mean wind speed at 100 m for all turbine locations (see Appendix Table 6.1) one can see that WindPRO predicts higher wind speeds than the other three models. Hence, that is why the total annual energy production (see Table 4.4) becomes larger for WindPRO than for OpenWind and STARCCM+, which have almost the same result. Examining more closely the differences between OpenWind and STARCCM+ (see Table 4.3), OpenWind

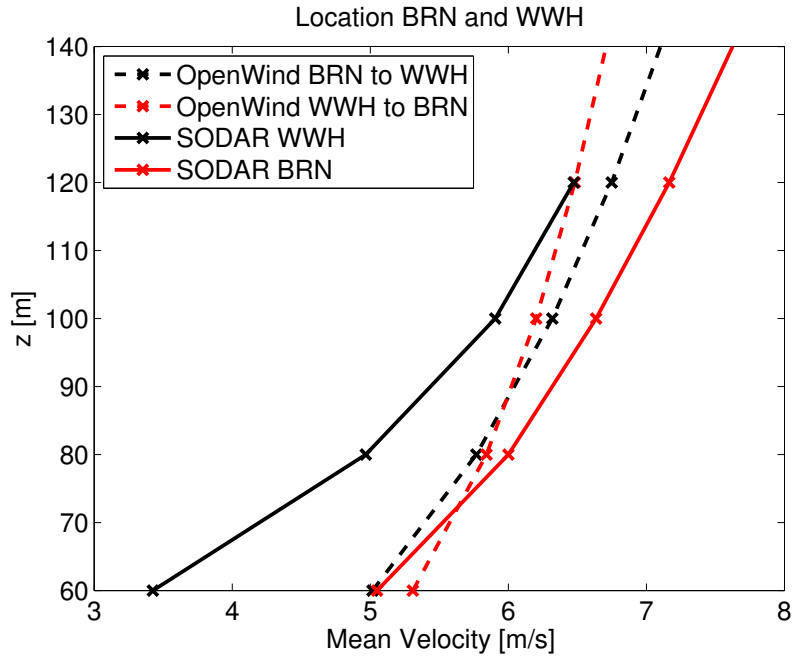


Figure 4.9: *Cross prediction in OpenWind. Wind profiles are simulated from SODAR WWH to SODAR BRN and from SODAR BRN to SODAR WWH.*

is found to not vary that much between the locations and at some locations the difference to STARCCM+ is significant (see for example wind turbine number T20). The RMSE (Table 4.5) between OpenWind and STARCCM+ is 157 MWh/year, which is quite small compared to the total annual production. Since OpenWind is not varying much between the wind turbines, the similarities with STARCCM+ in the total production can be seen as random.

Model	T4	T7	T8	T9	T11	T12	T13	T14	T15	T16	T17	T18	T20
OpenWind	5778	5650	5707	5638	5757	5479	5780	5721	5609	5524	5675	5703	5765
STARCCM+	5791	5518	5727	5532	5724	5256	5859	5789	5537	5590	5562	5795	6210
WindPRO	6470	6303	6119	5985	6101	5869	6173	6110	6120	6215	6180	6586	6471

Table 4.3: Annual predicted energy production for each wind turbine [MWh/year]. Comparison between OpenWind, STARCCM+ and WindPRO.

Model	Total Production [MWh/year]
OpenWind	73786
STARCCM+	73890
WindPRO	80702

Table 4.4: The total annual predicted energy production for all 13 wind turbines.

Model	RMSE [MWh/year]
OpenWind-STARCCM+	157

Table 4.5: The RMSE calculated as the difference between STARCCM+ and OpenWind for the 13 turbines.

5 Conclusion

In this study a comparison of the performance of three different models has been carried out. Each model had its own characteristics: OpenWind is a linear model, STARCCM+ is a CFD model and WRF is a mesoscale NWP model. Different settings were tested in OpenWind and STARCCM+ in order to improve the predictions and to test the models limitations. WeatherTech provided simulation results from the WRF model. The model results were compared to three different measurement time series from Skottfjället.

Based on the result, these conclusions have been made:

- The most accurate predictions are obtained from STARCCM+.
- If the landscape is homogeneous, WRF is able to predict the wind conditions.
- The increased roughness length of $z_0 = 2$ m for the forest gave the best result in both OpenWind and STARCCM+.
- By adding a displacement height of 20 m to the wind profile above a forest, the OpenWind result was further improved.
- The WRF model generally captures the wind shear although in most cases it overpredicts the wind speeds.
- Cross prediction and production estimation revealed that OpenWind shows very little differences between locations and is not able to capture the wind shear. Hence, the results of the OpenWind model are non-accurate for this type of terrain.
- The WRF model can be used with STARCCM+ to get a measurement independent solution.
- WindPRO predicts higher energy production than OpenWind and STARCCM+. The reason is that the meteorological mast, used by WindPRO, predicts higher wind speeds for the wind farm than the SODARs.

The measurement location of the WWH SODAR was not optimal, since it was placed within a valley. In future work it would be preferable to test cross predictions between two measurement locations with more homogeneous terrain. If further validations of the WRF models were performed, it could lead to that measurement campaigns are not needed to determine the wind resource of a location. Since the STARCCM+ simulation was limited to be able to run on a single computer, it could be interesting to compare these results with a much finer mesh. Furthermore, comparing the model predictions with an actual wind farm could increase the knowledge about the models and their accuracy.

6 Appendix A



Figure 6.1: *Installation of the WWH SODAR.*



Figure 6.2: *Installation of the BRN SODAR.*



Figure 6.3: *Installation of the meteorological mast.*

$$RMSE = \sqrt{\frac{1}{N} \sum_{i=1}^N (x_i - \hat{x}_i)^2} \quad (6.1)$$

where x_i is the modeled value and \hat{x}_i is the reference value.

Model	T4	T7	T8	T9	T11	T12	T13	T14	T15	T16	T17	T18	T20
OpenWind	6.9	6.8	6.9	6.8	6.9	6.7	6.9	6.9	6.8	6.8	6.9	6.9	6.9
STARCCM+	6.5	6.3	6.4	6.3	6.4	6.2	6.5	6.5	6.4	6.4	6.4	6.6	6.8
WRF	7.1	7.0	7.1	7.0	6.8	6.8	6.8	6.7	6.7	6.7	6.5	6.6	6.5
WindPRO	7.3	7.2	7.2	7.1	7.3	7.1	7.2	7.3	7.2	7.3	7.3	7.4	7.4

Table 6.1: Mean wind speed at 100 m given for all 13 wind turbines. All results are in m/s.

Model	Max [m/s]	Min [m/s]	Mean [m/s]
OpenWind	6.9	6.7	6.9
STARCCM+	6.8	6.2	6.5
WRF	7.1	6.5	6.8
WindPRO	7.4	7.1	7.3

Table 6.2: Maximum, minimum and mean wind speed at 100 m for all 13 wind turbine locations.

Setting Virtual Disk	Value
Power Curve	Table 3.4
Inner Radius	1 m
Outer Radius	45 m
Thickness	11 m
Coordinate system	Turbine coordinate system
Velocity Plane Radius	49.5 m
Velocity Plane Offset	4.5 m
Rotation Rate	14.9 rpm

Table 6.3: Setting for the virtual disk in STARCCM+ using 1D momentum. Except from the actual information from the wind turbine the setting for the virtual disk are specified according to the user guide for the 1D momentum method (CD-Adapco 2012).

References

- CD-Adapco (2010). *Windpark Siting Training CFD for Windpark Designers*. Tech. rep.
- (2012). *STARCCM+ User Guide 9.06.011*. Tech. rep.
- AQSystem (2013). *AQ500 windfinder User Guide*. Tech. rep.
- Bergström, H. et al. (2013). “Wind power in cold climates: Ice mapping methods”. In:
- Bowen, A. J. and N. G. Mortensen (1996). “Exploring the limits of WASP—the wind atlas analysis and application program”. In: *Riso-Contribution from the department of meteorology and wind energy to the EUWEC*, pp. 23–6.
- Corbett, J. et al. (2012). “CFD can consistently improve wind speed predictions and reduce uncertainty in complex terrain”. In: *European Wind Energy Conference*.
- Davidson, L. (2011). “Fluid mechanics, turbulent flow and turbulence modeling”. In: *Chalmers University of Technology, Goteborg, Sweden (Nov 2011)*.
- Dellwik, E., J. Arnqvist, et al. (2014). “Meso-scale modeling of a forested landscape”. In: *Journal of Physics: Conference Series*. Vol. 524. 1. IOP Publishing, p. 012121.
- Dellwik, E., L. Landberg, and N. O. Jensen (2006). “WASP in the Forest”. In: *Wind Energy* 9.3, pp. 211–218.
- Emeis, S. (2012). *Wind Energy Meteorology: Atmospheric Physics for Wind Power Generation*. Springer Science & Business Media.
- Holton, J. R. and G. J. Hakim (2013). *An introduction to dynamic meteorology*. Academic press.
- Lantmäteriet (2013). *Produktbeskrivning: GSD-Terrängkartan vektor*. Tech. rep.
- Mandas, N. et al. (2004). “Numerical simulation of the Atmospheric Boundary Layer (ABL) over complex terrains”. In: *Proceedings from EWEC*.
- Manning, J. et al. (2011). *Validation and challenges of CFD in complex terrain for real world wind farms*.
- Metria (2015). *Höjddata Metria*. URL: <http://www.metria.se/Vara-erbjudanden/Kartor-och-bilder/Metria-som-geodataleverantor/Hojddata/> (visited on 06/14/2015).
- Mortensen, N. G. et al. (1993). “Wind atlas analysis and application program (WASP)”. In:
- Phillips, G. and R. Traci (1979). “A preliminary users guide for the NOABL objective analysis code”. In: *Report from Science Applications, Inc. La Jolla, California, USA*.
- SCB (2014). *Tillförsel och användning av el 2001-2013*. URL: http://www.scb.se/sv_/Hitta-statistik/Statistik-efter-amne/Energi/Tillforsel-och-anvandning-av-energi/Arlig-energistatistik-el-gas-och-fjarrvarme/6314/6321/24270/ (visited on 11/28/2014).
- Skamarock, W. C. et al. (2005). *A description of the advanced research WRF version 2*. Tech. rep. DTIC Document.
- SLU (2015a). *Lantmäteriet: Vägkarta Vector*. URL: <http://maps.slu.se/> (visited on 03/20/2015).
- (2015b). *Skogskartan SLU*. URL: <http://gisweb.slu.se/knngrund/> (visited on 05/20/2015).
- Stuart, P. (2004). “The use of CFD in wind farm development”. In: *Hydraulic aspects of renewable energy* 30.
- Stull, R. B. (1988). *An introduction to boundary layer meteorology*. Vol. 13. Springer Science & Business Media.
- Svensson, U. and K. Häggkvist (1990). “A two-equation turbulence model for canopy flows”. In: *Journal of Wind Engineering and Industrial Aerodynamics* 35, pp. 201–211.
- SWPTC (2015). *Swedish Wind Power Technology Center*. URL: <http://www.chalmers.se/ee/swptc-sv> (visited on 06/14/2015).
- Tomkins, O. (2007). “Validation of SODAR measurements on a complex, forested site”. In:
- Troen, I. and E. Lundtang Petersen (1989). “European wind atlas”. In:
- Truepower, A. (2010). “openWind-Theoretical basis and validation. Version 1.3”. In: *AWS Truepower, LLC, USA*.
- Versteeg, H. K. and W. Malalasekera (2007). *An introduction to computational fluid dynamics: the finite volume method*. Pearson Education.
- Vestas (2010). *General Specification V90-1.8/2.0 MW 50Hz VCS*. Tech. rep. Technology R and D.